Article:
Li, H. and Zhu, Z.Q. (2019) Optimal number of magnet pieces of flux reversal permanent magnet machines. IEEE Transactions on Energy Conversion, 34 (2). pp. 889-898. ISSN: 0885-8969

https://doi.org/10.1109/TEC.2018.2866765

Optimal Number of Magnet Pieces of Flux Reversal Permanent Magnet Machines

H. Y. Li, *Student Member, IEEE*, and Z.Q. Zhu, *Fellow, IEEE*

***Abstract*—This paper aims to comprehensively analyze the influence of number of permanent magnet (PM) pieces on electromagnetic performance of flux reversal permanent magnet (FRPM) machines. Firstly, the unified analytical model of FRPM machines having different numbers of PM pieces is established, from which the optimal number of PM pieces and the corresponding rotor pole number can be identified. It shows that by employing the optimal number of PM pieces instead of the conventional two on each stator tooth, additional back-EMF component can be generated which is beneficial to boost the machine performance. Then, the influence of critical design parameters including stator slot opening ratio, split ratio and stator slot number is investigated, providing a guidance to the design of FRPM machines aiming at maximum output torque. In addition, both finite element analyses and experimental tests are conducted to verify the analytical analyses. For 6-slot-stator FRPM machines, experimental results show that more than 40% higher output torque can be achieved in the machine with optimal number of PM pieces when compared to the conventional one.**

***Index Terms*—Analytical model, flux reversal, permanent magnet (PM), working harmonic**

I. Introduction

With the help of high-energy permanent magnet (PM) materials, the PM machines have now been widely used in various industrial applications, thanks to their superior torque density, efficiency, and topology diversity [1-3]. For low-speed and high-torque applications such as wind power, marine propulsion and rail traction etc., the direct-drive PM machines are regarded as promising candidates due to their simplified mechanical structure, high reliability, and less vibration and noise. To reduce the overall volume of the direct-drive system, numerous PM machine topologies toward high torque density have been proposed and can be divided into several categories based on their configuration or working principle, such as stator-PM machines [4], transverse flux machines [5], magnetic gear integrated machines [6], Vernier machines [7], partitioned stator machines [8], and so on. Among these machines, stator-PM machines exhibit inherent merits of efficient heat management and robust rotor structure, thus attracting much attention nowadays.

According to different placements of PMs, there are mainly three kinds of stator-PM machines which are doubly salient PM (DSPM) machine [9], switched flux PM (SFPM) machine [10] and flux reversal PM (FRPM) machine [11], respectively. In comparison with other two kinds of machines, the FRPM machine is of surface-mounted PM (SPM) structure, making its stator structure less complex. However, the torque density of the FRPM machine tends to be smaller than the SFPM machine because of the larger equivalent air-gap length for rotor tooth modulation [4]. Therefore, the torque improvement of the FRPM machine is of great significance to boost its competitiveness against other machines and broaden its application prospect.

Up to now, a few papers have provided some approaches to improve the torque of the FRPM machine. In [12], different winding configurations of the FRPM machine are analyzed. It states that the 6/14 stator slot/rotor pole FRPM machine with full-pitch distributed winding has 50% higher torque than its counterpart with concentrated winding. In [13], the optimal rotor pole number of the FRPM machine is revealed based on analytical equations. It shows that the 14-pole-rotor is preferred for the 12-slot-stator. In [14], the stator of the FRPM machine is split into two stators to separate the PM and armature winding. It is proven that the proposed 12/10 machine enlarges the torque by 56% due to its better utilization of inner space.

Besides, the PM configuration of the FRPM machine has also been investigated from the following several aspects: 1) the SPM structure can be replaced by inset-PM structure [15] or consequent-pole PM (CPM) structure, e.g. the torque of a 12/16 FRPM machine with CPM structure is improved by 25% in [16]; 2) the PMs can be evenly arranged along the entire inner surface of the stator instead of mounting on the inner surface of each stator tooth only, e.g. by evenly arranging 36-pole PMs on the inner stator surface of a 12/17 FRPM machine, its torque can be improved by 33% [17]; 3) the polarities of two adjacent magnets on different stator teeth can be either identical or opposite, e.g. in [18], 17% higher torque of a 12/14 FRPM machine is obtained by simply adjusting the two adjacent magnets belonging to two stator teeth from identical poles to opposite poles.

In addition to the three aspects aforementioned, the FRPM machines with increased number of PM pieces have also been proposed and analyzed. Most typically, two PM pieces are mounted on each stator tooth of the FRPM machine [19], as shown in Fig. 1(a) (taking the 6-slot-stator FRPM machine for instance). In [20], the FRPM machine with increased PM pieces is firstly proposed, viz., four PM pieces instead of two, are mounted on each stator tooth, as shown in Fig. 1(b). Ideally,

The authors are with the Department of Electronic and Electrical Engineering, The University of Sheffield, Sheffield S1 4DE, U.K. (e-mail: hli53@ sheffield.ac.uk; z.q.zhu@ sheffield.ac.uk).

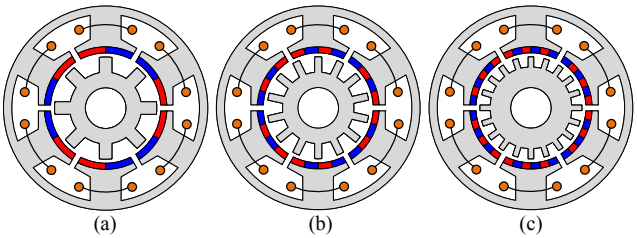

Fig. 1. FRPM machines with different numbers of magnet pieces. (a) Conventional FRPM machine with *npp*=1. (b) *npp*=2. (c) *npp*=3.

2*npp* PM pieces can be mounted on each stator tooth, where *npp* is the number of PM pairs with minimum value being 1. Aiming at low-speed servo applications, a 12/28 FRPM machine with *npp*=2 is optimized and analyzed in [20]. Although the working principle and winding configuration of this kind of FRPM machine are then investigated in some other papers [12] [21], its performance difference against the conventional FRPM machine with *npp*=1 has never been addressed. In addition, the analysis of the FRPM machine with *npp*>2 has not been found in existing papers either. For instance, Fig. 1(c) shows the FRPM machines with six PM pieces on each stator tooth (*npp*=3).

Therefore, this paper aims to provide a unified analysis and comparison of FRPM machines having different numbers of PM pieces on each stator tooth. More importantly, the optimal number of PM pieces can be identified, which is beneficial to improve the machine performance. To obtain a generalized conclusion, the determination of the optimal number of PM pieces, and the influence of design parameters including stator slot opening ratio, split ratio, and stator slot number will be investigated by means of analytical method. Both finite element analyses (FEA) and experiments are used to validate the conclusions and findings.

II. Machine Configuration and Operation Principle

A. Machine Configuration

The most typical configuration of a three-phase FRPM machine is shown in Fig. 1(a). As can be seen, the rotor of the FRPM machine is of pure reluctance structure, which has improved mechanical strength and is easy for manufacturing even if with high pole number. The non-overlapping concentrated armature windings are always wound around the stator teeth, resulting in short end-winding. Also, a pair of PMs is mounted on the inner surface of each stator tooth. With rotor rotating, the flux through the armature winding varies and the PM induced back-electromotive force (EMF) interacts with the injected armature current to produce torque. It should be noted that the polarities of two adjacent PM pieces belonging to two stator teeth can be either identical or opposite. In the case of identical polarities, the number of stator slot can be only even while that can be either even or odd in the case of opposite polarities [18].

B. Analytical Derivation of Machine Performance

To investigate the operation principle of a FRPM machine and the influence of different numbers of PM pieces, the analytical derivation of machine performance is conducted. To simplify the analysis, some assumptions are made as: 1) the saturation of the stator and rotor core is neglected; 2) the end-effect and fringing effect of the machine are neglected; 3) the magnets are radially-magnetized; 4) the dimensions of all PM pieces are the same.

For simplicity, the analytical expressions are deduced based on the FRPM machine with polarities of two adjacent PM pieces belonging to two stator teeth being opposite, and its schematic is shown in Fig. 2. Some critical dimensional parameters including overall diameter (D), inner radius of stator (R_{si}), stator slot pitch (τ_s), width of stator slot opening (w_{so}), PM height (h_m), air-gap length (g), rotor pole pitch (τ_r), and width of rotor slot opening (w_{ro}) are labeled.

By using simple magnetomotive force (MMF)-permeance model [22] [23], the no-load air-gap flux density can be given as

$$B(\theta,t) = F_{PM}(\theta)\Lambda_r(\theta,t) \tag{1}$$

where $F_{PM}(\theta)$ is the PM MMF which is static under the stator reference frame, and $\Lambda_r(\theta,t)$ is the specific air-gap permeance produced by the salient rotor which is dynamic due to the rotor rotation.

Considering the PM MMF of the machine, it is directly determined by the number of PM pairs (*npp*) on each stator tooth and the corresponding magnetization directions. As shown in Fig. 2, since the PM arrangements of any two stator teeth are exactly the same, the PM MMFs are periodically distributed in the air-gap with a period T of τ_s. By assuming the magnetization direction of the 1st magnet piece outward, the PM MMF waveforms of different *npp* (1 to 3) are shown in Fig. 3.

The PM MMF can then be expressed in Fourier series, as

$$F_{PM}(\theta) = \sum_{i=1,2,3\cdots}^{\infty} F_i \sin(iN_s\theta) \tag{2}$$

where N_s is the number of stator slots, i is the order of Fourier series, F_i is the corresponding Fourier coefficient and is

$$F_i = \frac{4F}{TiN_s}\left[-1-(-1)^{npp}\cos(iN_s k\frac{T}{2}) + \sum_{j=1,2\cdots}^{npp+1} 2(-1)^{j-1}\cos(iN_s\frac{j-1}{npp}k\frac{T}{2})\right] \tag{3}$$

where $T=\tau_s=2\pi/N_s$, $k=(1-w_{so}/\tau_s)$, F is related to the remanence (B_r), height (h_m), and relative permeability (μ_r) of the PM material, and $F=B_r h_m/\mu_r\mu_0$.

As for air-gap permeance, it can also be expressed in Fourier series, as

$$\Lambda_r(\theta,t) = \sum_{q=0,1,2\cdots}^{\infty} \Lambda_q \cos\left[qN_r(\theta-\theta_0-\Omega_r t)\right] \tag{4}$$

and the Fourier coefficients can be obtained as [24]

$$\Lambda_0 = \frac{\mu_0}{g'}(1-1.6\beta\frac{w_{ro}}{\tau_r}) \tag{5}$$

$$g' = g + h_m/\mu_r \tag{6}$$

$$\Lambda_q = -\beta\frac{4}{\pi q}\frac{\mu_0}{g'}\left[\frac{1}{2}+\frac{(qw_{ro}/\tau_r)^2}{0.78125-2(qw_{ro}/\tau_r)^2}\right]\sin(1.6\pi q\frac{w_{ro}}{\tau_r}) \tag{7}$$

$$\beta = \frac{1}{2}\left[1-\frac{1}{\sqrt{1+(w_{ro}/2g')^2}}\right] \tag{8}$$

where Ω_r is the angular speed of the rotor, N_r is the rotor pole

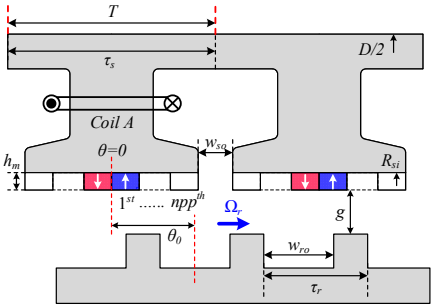

Fig. 2. PM arrangement and parameters of the FRPM machine.

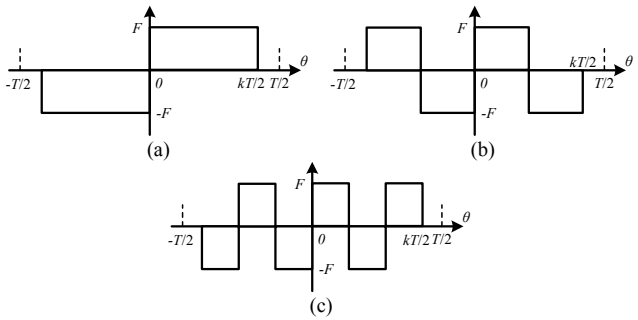

Fig. 3. PM MMF of FRPM machines. (a) *npp*=1. (b) *npp*=2. (c) *npp*=3.

number, q is the order of Fourier series, and Λ_q is the corresponding Fourier coefficient.

The no-load air-gap flux density can then be expressed as

$$B(\theta,t)=\Lambda_0\sum_{i=1,2,3\cdots}^{\infty}F_i\sin(iN_s\theta)+\sum_{i=1,2,3\cdots}^{\infty}\sum_{q=1,2,3\cdots}^{\infty}\frac{1}{2}F_i\Lambda_q\sin[(iN_s\pm qN_r)\theta\mp qN_r(\theta_0+\Omega_r t)] \tag{9}$$

From (1)-(9), it can be seen that abundant air-gap flux density harmonics exist due to the rotor tooth modulation and the magnitudes of these harmonics highly depend on *npp*.

Considering the cogging torque of the machine, by using the virtual work method, it can be given as

$$T_c=-\frac{\partial W_c}{\partial\alpha}=-\frac{\partial W_c}{\partial(\Omega_r t)} \tag{10}$$

where α is the rotor rotational angle, and W_c is the magnetic field energy which is equal to the co-energy stored in the air-gap and PMs of the machine under the assumption of infinite permeability of stator and rotor core, as

$$\begin{aligned}W_c(t)&=\int\frac{1}{2\mu_0}B(\theta,t)^2dV=\int\frac{1}{2\mu_0}F_{PM}(\theta)^2\Lambda_r(\theta,t)^2dV\\&=\frac{l(R_{si}^2-R_{ro}^2)}{2\mu_0}\int_0^{2\pi}F_{PM}(\theta)^2\Lambda_r(\theta,t)^2d\theta\\&=\frac{\pi l(R_{si}^2-R_{ro}^2)}{4\mu_0}\sum F_{\frac{nN_r}{N_s}}'\Lambda_n'\cos[nN_r(\theta_0+\Omega_r t)]\end{aligned} \tag{11}$$

where l is axial length of the machine, R_{ro} is the outer radius of rotor, F' is the Fourier coefficient of $F_{PM}(\theta)^2$, Λ' is the Fourier coefficient of $\Lambda_r(\theta,t)^2$, and n is the integer which makes (nN_r/N_s) an integer as well.

Then the cogging torque can be deduced as

$$T_c(t)=\frac{nN_r\pi l(R_{si}^2-R_{ro}^2)}{4\mu_0}\sum F_{\frac{nN_r}{N_s}}'\Lambda_n'\sin[nN_r(\theta_0+\Omega_r t)] \tag{12}$$

The fundamental period of the cogging torque, N_c, is equal to the minimum n, and can be expressed as

$$N_c=n_{\min}=\frac{N_s}{GCD(N_r,N_s)} \tag{13}$$

From (13), it can be found that N_c is only related to N_s and the greatest common divisor (GCD) between N_r and N_s, and is irrelevant to *npp*. This is because that the waveforms of $F_{PM}(\theta)^2$ are all the same regardless of *npp*, as shown in Fig. 3.

As shown in Fig. 2, considering the flux through Coil A,

$$\begin{aligned}\lambda_A(t)&=n_c\int B(\theta,t)ds=n_clR_{si}\int_{-k\pi/N_s}^{k\pi/N_s}B(\theta,t)d\theta\\&=\sum_{i=1,2,3\cdots}^{\infty}\sum_{q=1,2,3\cdots}^{\infty}\frac{n_clR_{si}F_i\Lambda_q}{(iN_s\pm qN_r)}\sin\left[\left(\frac{iN_s\pm qN_r}{N_s}\right)k\pi\right]\cdot\\&\quad\sin[\mp qN_r(\theta_0+\Omega_r t)]\end{aligned} \tag{14}$$

where n_c is the number of series-connected turns of Coil A.

Correspondingly, the back-EMF of Coil A can be obtained as

$$e_A(t)=-\frac{d\lambda_A(t)}{dt}=\sum_{i=1,2,3\cdots}^{\infty}\sum_{q=1,2,3\cdots}^{\infty}\frac{\pm n_clR_{si}F_i\Lambda_q qN_r\Omega_r}{(iN_s\pm qN_r)}\cdot\sin\left[\left(\frac{iN_s\pm qN_r}{N_s}\right)k\pi\right]\cos[qN_r(\theta_0+\Omega_r t)] \tag{15}$$

From (15), it can be seen that the air-gap flux density harmonics with the same q contribute to the back-EMF of the same frequency. Since Λ_1 is much larger than the magnitudes of other permeance harmonics, the flux density harmonics with order being $(iN_s \pm N_r)$ are all possible to produce the fundamental back-EMF, of which the magnitude can be expressed as

$$E_A=\sum_{i=1,2,3\cdots}^{\infty}\frac{\pm n_clR_{si}F_i\Lambda_1N_r\Omega_r}{(iN_s\pm N_r)}\sin\left[\left(\frac{iN_s\pm N_r}{N_s}\right)k\pi\right] \tag{16}$$

Obviously, the back-EMF is greatly influenced by *npp* because the magnitudes of the air-gap flux density harmonics are related to *npp*, as seen from (3) and (9).

Since the reluctance torque of FRPM machine is negligible [3], the average torque of the machine can be derived as

$$\begin{aligned}T&=\frac{3}{2}n_{coil}k_dI_AE_A\\&=\frac{3}{2}n_{ph}k_dI_A\sum_{i=1,2,3\cdots}^{\infty}\frac{\pm lR_{si}F_i\Lambda_1N_r\Omega_r}{(iN_s\pm N_r)}\sin\left[\left(\frac{iN_s\pm N_r}{N_s}\right)k\pi\right]\end{aligned} \tag{17}$$

where n_{coil} is the number of series-connected coils per phase, n_{ph} is the number of series-connected turns per phase, k_d is the distribution factor of the armature winding, and I_A is the peak value of the phase current.

III. Analysis of FRPM Machines with Different Numbers of PM Pieces

A. Optimal Rotor Pole Number

It is clear that the rotor pole number has a big influence on the performance of FRPM machines. In terms of torque density, it has been proven that the 14-pole-rotor is suitable for the

TABLE I
FIXED PARAMETERS OF THE MACHINES

Parameters	Value	Parameters	Value
Overall diameter (D)	90mm	Axial length (l)	25mm
Inner radius of stator (R_{si})	31.5mm	Width of stator slot opening (w_{so})	2.5mm
PM height (h_{mi})	2mm	Air-gap length (g)	0.5mm
Width ratio of rotor pole (w_{ro}/τ_r)	0.7	Number of turns per coil (n_c)	1
Remanence of PM (B_r)	1.2T	Relative permeability of PM (μ_r)	1.05

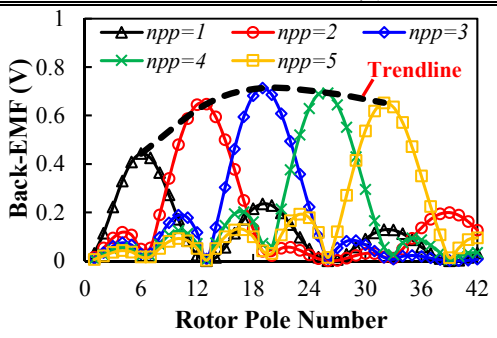

Fig. 4. Magnitudes of the fundamental back-EMFs with different rotor pole numbers. ($\Omega_r = 2\pi \cdot 4000/60$ rad/s)

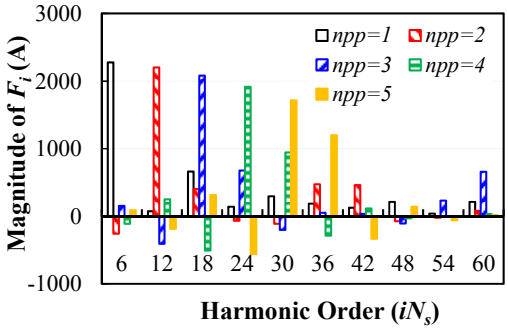

Fig. 5. Harmonic spectra of the PM MMFs.

12-slot-stator FRPM machine when npp=1 [13] [18]. However, for different npp, the most suitable rotor pole number varies, which will be illustrated in the following.

Based on the analytical expressions and the fixed parameters listed in TABLE I, the magnitude of the fundamental back-EMF is used to evaluate the torque performance of the FRPM machines with different stator slot/rotor pole combinations. Fig. 4 shows the variation of the magnitude of the fundamental back-EMF against rotor pole number when N_s=6. When npp ranges from 1 to 5, the optimal N_r are 6, 13, 19, 26, and 32, respectively. This is because that the variation of flux is caused by the relative movement between rotor poles and PM pieces, a similar number of rotor pole and fundamental pole-pair of PM MMF is beneficial to fully utilize the PM field. Fig. 5 shows the harmonic spectra of the PM MMF. As can be seen, the harmonic order of the largest magnitude is related to npp, which is $nppN_s$. In addition, from (16), the back-EMF of the machine with a large N_r tends to be high when the rotor speed is fixed. Therefore, the optimal rotor pole number N_r should be ($nppN_s$+m), where m= 0, 1 or 2. Considering the fact that the unbalanced magnetic force exists if N_r is odd, the suggested rotor pole number for a three-phase FRPM machine can be given as

$$N_r = nppN_s + 2 \tag{18}$$

B. Identification of Working Harmonics of PM MMF

Considering the maximum back-EMF value of the FRPM machines with different npp (see the trend line in Fig. 4), when npp increases from 1, the back-EMF firstly increases and then reaches a maximum with npp=3, and it starts to decrease by further increasing npp. In comparison with the conventional FRPM machine with npp=1, the back-EMF of the FRPM machine with npp=3 is improved by 61%.

To identify the best npp for the FRPM machine, and also explain the trend line of the performance variation against npp, it is necessary to quantify the contribution of each harmonic of the PM MMF. From (16), it is shown that the fundamental back-EMF is contributed by several PM MMF harmonics but with different weight factors, as

$$E_A \propto \sum_{i=1,2,3\cdots}^{\infty} \frac{\pm N_r \Lambda_1}{(iN_s \pm N_r)} \sin\left[\left(\frac{iN_s \pm N_r}{N_s}\right)k\pi\right] F_i \propto \sum_{i=1,2,3\cdots}^{\infty} f_w^i F_i \tag{19}$$

The weight factor f_w^i of the iN_s^{th} MMF harmonic can be defined as

$$f_w^i = \frac{N_r \Lambda_1}{(iN_s + N_r)} \sin\left[\left(\frac{iN_s + N_r}{N_s}\right)k\pi\right] - \frac{N_r \Lambda_1}{(iN_s - N_r)} \sin\left[\left(\frac{iN_s - N_r}{N_s}\right)k\pi\right] \tag{20}$$

Under the fixed parameters listed in TABLE I and the suggested rotor pole number in (18), the weight factor f_w^i of the 6-slot-stator FRPM machines with different npp can be calculated, as shown in Fig. 6. Not surprisingly, for each npp, the weight factor of the $nppN_s^{th}$ harmonic is the highest. Therefore, the fundamental back-EMF of the machine is largely resulted from the $nppN_s^{th}$ PM MMF since its magnitude is also the highest, as shown in Fig. 5. The $nppN_s^{th}$ PM MMF is then defined as *Principal* MMF in this paper. In addition to *Principal* MMF, it is found that both weight factor and magnitude of the $(npp+1)N_s^{th}$ PM MMF are considerable especially when npp is large. The $(npp+1)N_s^{th}$ PM MMF is then defined as *Auxiliary* MMF. TABLE II shows the back-EMF contribution from both *Principal* and *Auxiliary* MMFs. For each npp, by setting the back-EMF produced by *Principal* MMF as benchmark, the normalized back-EMF produced by *Auxiliary* MMF is listed as well. It shows that the back-EMF contribution of *Auxiliary* MMF increases with npp, e.g. when npp =1, it is only 2% of the back-EMF produced by *Principal* MMF while it grows to 36% for npp=5. More importantly, the back-EMF resulted from these two MMF components accounts for more than 90% of the overall back-EMF. Therefore, it can be regarded that the back-EMF as well as the torque of the studied FRPM machines are mainly contributed by two working harmonics of the PM MMF, i.e. the $nppN_s^{th}$ and the $(npp+1)N_s^{th}$.

The back-EMFs produced by these two working harmonics are shown in Fig. 7, and can be used to explain the trend of the performance variation against npp. It can be seen that the back-EMF produced by *Principal* MMF firstly increases with npp thanks to the increased weight factor shown in Fig. 6, and then it decreases due to the decreased magnitude as shown in Fig. 5. It achieves a maximum when npp=3. In terms of the back-EMF produced by *Auxiliary* MMF, it always increases

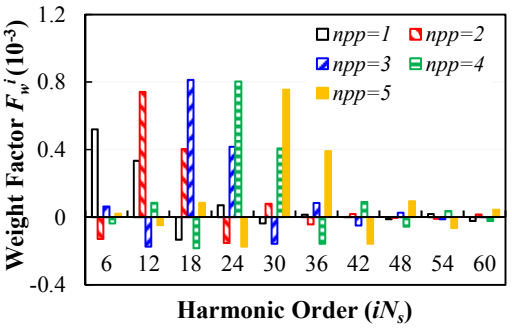

Fig. 6. Weight factors of the PM MMF harmonics.

TABLE II
BACK-EMF CONTRIBUTION OF *PRINCIPAL* AND *AUXILIARY* MMFS

npp	Overall Back-EMF	Produced by *Principal* MMF	Produced by *Auxiliary* MMF	Produced by other MMF harmonics
1	0.36V	0.38V (100%)	0.01V (2%)	-0.03V
2	0.59V	0.54V (100%)	0.05V (10%)	0
3	0.69V	0.56V (100%)	0.09V (17%)	0.04V
4	0.69V	0.51V (100%)	0.13V (25%)	0.05V
5	0.65V	0.43V (100%)	0.16V (36%)	0.06V

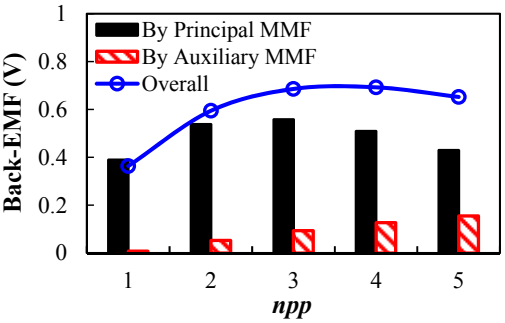

Fig. 7. Back-EMF produced by *Principal* MMF and *Auxiliary* MMF.

with *npp* since the magnitude of *Auxiliary* MMF largely increases with *npp*, as shown in Fig. 5. On the whole, when *npp* increases from 1, the performance of the FRPM machine is firstly improved due to the additional contribution of *Auxiliary* MMF. With the further increase of *npp*, the machine performance deteriorates due to the magnitude reduction of *Principal* MMF. Therefore, there exists an optimal *npp* for FRPM machine, and it is 3 when N_s=6.

C. Influence of npp on Cogging Torque

From (13), it is found that the fundamental period of cogging torque is determined by N_s and N_r. Although the optimal N_r varies with *npp* based on (18), the GCD (N_s, N_r) remains unchanged when N_s=6. Therefore, *npp* only affects the peak to peak value of the cogging torque, as shown in Fig. 8. The cogging torque decreases when *npp* increases from 1 to 4. In comparison with *npp*=4, the cogging torque with *npp*=5 is larger. As shown in Fig. 3, the waveforms of $F_{PM}(\theta)^2$ are exactly the same for different *npp*. However, for different *npp*, the cogging torque is related to different harmonics of $F_{PM}(\theta)^2$, of which the order can be obtained from (12) and is (3*npp*+1) when N_s=6. Fig. 9 shows the absolute value of harmonic magnitude of $F_{PM}(\theta)^2$, and the harmonics contributing to the fundamental cogging torques of different *npp* are also labeled. As can be seen, the magnitude variation of these harmonics

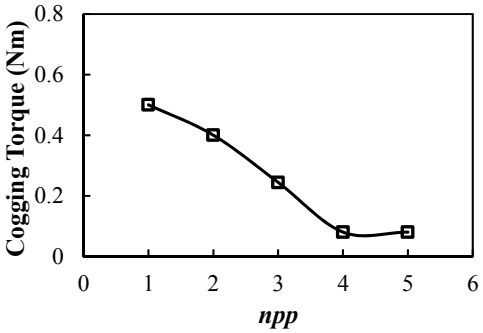

Fig. 8. Peak to peak values of the cogging torques with different *npp*.

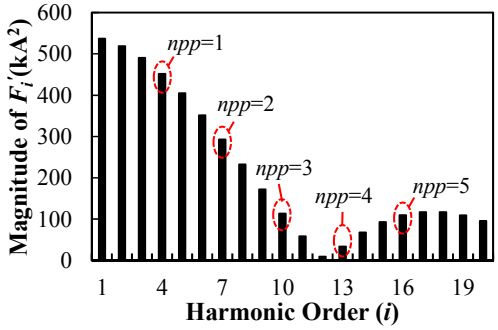

Fig. 9. Magnitudes of harmonics of $F_{PM}(\theta)^2$.

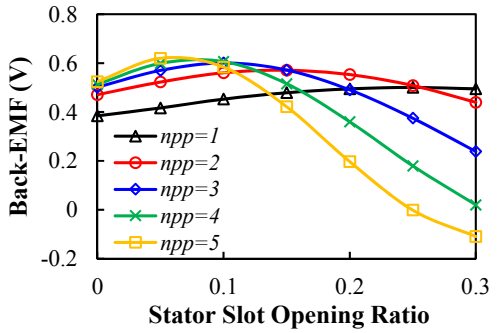

Fig. 10. Magnitudes of the fundamental Back-EMFs with different w_{so}/τ_s.

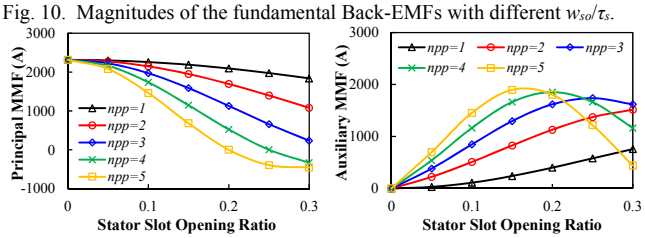

Fig. 11. Magnitude variation of PM MMF against stator slot opening ratio. (a) *Principal* MMF. (b) *Auxiliary* MMF.

matches well with the cogging torque variation in Fig. 8.

IV. INFLUENCE OF DESIGN PARAMETERS

To provide a simple design guidance of the FRPM machines analyzed above, the influence of some key design parameters on the machine performance is investigated.

A. Stator Slot Opening Ratio

Since the ratio of stator slot opening to stator slot pitch (w_{so}/τ_s) (designated as stator slot opening ratio) has a big influence on the distribution of the PM MMF, its influence on the machine performance is firstly investigated while other

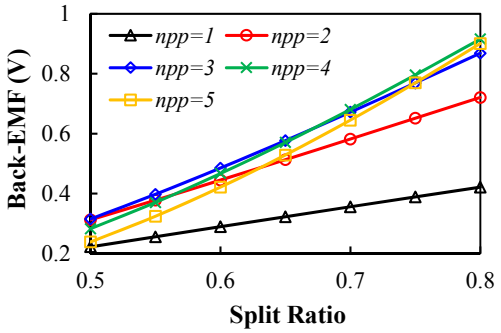

Fig. 12. Magnitudes of the fundamental back-EMFs with different split ratios.

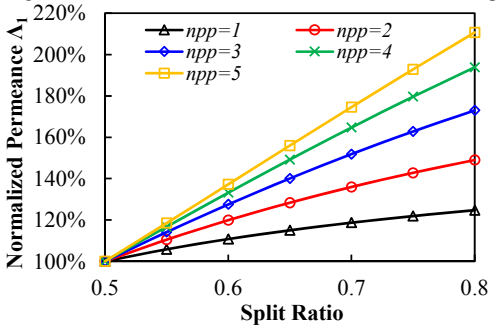

Fig. 13. Variation of normalized permeance Λ_1 against split ratio.

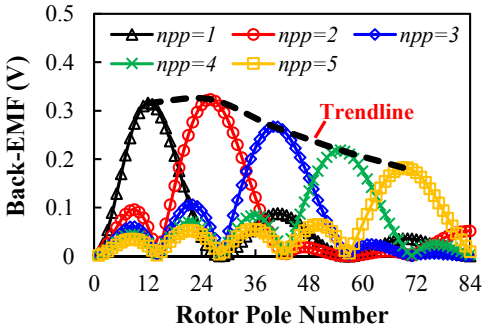

Fig. 14. Fundamental back-EMF variation against rotor pole number (N_s=12).

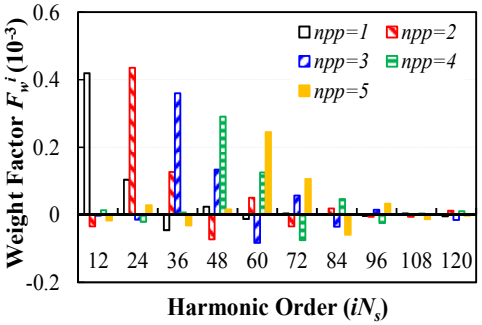

Fig. 15. Weight factors of PM MMF for N_s=12.

parameters are kept the same as TABLE I. Fig. 10 shows the variation of the magnitude of the fundamental back-EMF against w_{so}/τ_s. As can be seen, for each *npp*, there exists an optimal stator slot opening ratio and it decreases with *npp*. For instance, the optimal width ratio is 0.25 when *npp*=1 while that is 0.1 when *npp*=3. To further explain this phenomenon, Fig. 11 shows the magnitude variation of both *Principal* MMF and *Auxiliary* MMF. When the ratio (w_{so}/τ_s) increases from 0 to 0.3, the magnitude of *Principal* MMF decreases regardless of *npp*. It means that the back-EMF produced by *Principal* MMF decreases with the ratio. In contrast, the magnitude of *Auxiliary* MMF as well as the corresponding back-EMF component tend to increase with the ratio, but there exists an optimal value for *npp*>2. Considering different *npp*, the sensitivity of the PM MMF to the ratio is the lowest for *npp*=1 and it increases with *npp*. Therefore, the optimal stator slot opening ratio is relatively large for *npp*=1 since it tends to utilize more *Auxiliary* MMF due to the high weight factor shown in Fig. 6. When *npp* increases, the optimal ratio becomes smaller since the *Principal* MMF rapidly decreases with the ratio and the optimal ratio for Auxiliary MMF also decreases.

B. Split Ratio

It is well-known that there should be an optimal split ratio for PM machines due to the tradeoff between the magnetic loading and electric loading. To simplify the analysis of the influence of *npp* on the optimal value of split ratio, only the variation of back-EMF, *viz.* the equivalent electric loading against split ratio is calculated by assuming the number of turns per coil n_c and other parameters unchanged as TABLE I. As shown in Fig. 12, for all *npp*, the fundamental back-EMFs increase against split ratio but with different rates of increase, and the rate of increase is larger for a larger *npp*. Therefore, in comparison with the small *npp*, the optimal split ratio should be larger for the large *npp*. This can be further explained by the variation of the fundamental permeance Λ_1 from (20), since the back-EMF is proportional to Λ_1 which is related to N_r. For each *npp*, taking Λ_1 with split ratio being 0.5 as benchmark, the variation of the normalized Λ_1 against split ratio is shown in Fig. 13. As can be seen, the increase rate is larger for a larger *npp*, and is consistent with the variation of fundamental back-EMF shown in Fig. 12.

TABLE III
OPTIMAL *NPP* FOR DIFFERENT NUMBERS OF STATOR SLOT

N_s	6	12	18	24
Optimal *npp*	3	2	1	1

C. Stator Slot Number

For FRPM machines with different numbers of stator slot, the influence of *npp* is also investigated. Fig. 14 shows the variation of the magnitude of the fundamental back-EMF against rotor pole number when N_s=12. Similar to Fig. 4, there is an optimal rotor pole number for each *npp*, and it is basically consistent with (18).

For N_s=6, it has been proven that by increasing *npp* from 1 to the optimal value of 3, the back-EMF can be effectively improved mainly due to the increased weight factor of *Principal* MMF in Fig. 6, and increased magnitude of *Auxiliary* MMF in Fig. 5. However, for N_s=12, the optimal *npp* is 2 instead of 3, which can be observed from Fig. 14. This can be explained by the weight factor shown in Fig. 15. Compared with that shown in Fig. 6, *npp*=2 has the highest weight factor of *Principal* MMF, and it drops rapidly with *npp*.

Similarly, the optimal *npp* for other N_s is identified and listed in TABLE III. As can be seen, the optimal *npp* becomes 1 when N_s>12, i.e. the torque density of the machines cannot be

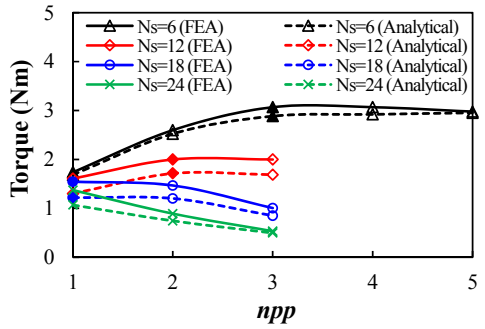

Fig. 16. Torque variation against *npp*.

TABLE IV
PARAMETERS OF OPTIMUM MODELS AND PROTOTYPES (N_s=6)

Parameters	FEA models					Prototypes		
npp	1	2	3	4	5	1	2	3
Overall diameter (D, mm)	90							
Axial length (l, mm)	25							
Split ratio ($2R_{si}/D$)	0.63	0.66	0.7	0.71	0.74	0.65		
Width ratio of stator slot opening (w_{so}/τ_s)	0.23	0.13	0.1	0.07	0.05	0.08		
Stator yoke thickness (h_{sy}, mm)	3.1	3.3	3.3	3.4	3.2	4.2		
Width of stator tooth (w_{st}, mm)	12.3	7.4	7.5	8.9	8.5	8.4		
PM height (h_{mi}, mm)	2	2	2	2	2	2		
Width ratio of rotor pole (w_{ro}/τ_r)	0.67	0.72	0.76	0.75	0.75	0.75	0.7	0.7

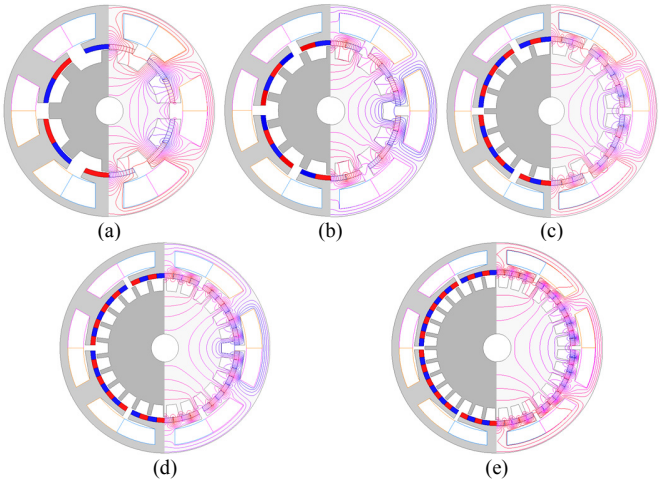

Fig. 17. Cross-sections and flux distributions. (a) *npp*=1. (b) *npp*=2. (c) *npp*=3. (d) *npp*=4. (e) *npp*=5.

improved by increasing the number of PM pieces on each stator tooth. This can be explained by the limited stator slot pitch under the fixed stator outer diameter D (90mm in this study).It should be noted that the optimal *npp* may vary with D. However, for different D, the optimal *npp* can still be determined and analyzed by using the analytical model in this paper.

V. PERFORMANCE VALIDATION BY FEA

To verify the findings obtained by analytical model, the genetic-algorithm-based global optimization by FEA is implemented for all FRPM machines with different *npp*. To achieve a fair comparison, all machines are optimized under the same effective space envelop (D=90mm and l=25mm) and copper loss (p_{cu}= 20W). Fig. 16 shows the torque variation against *npp*. Apart from the results obtained by FEA, the

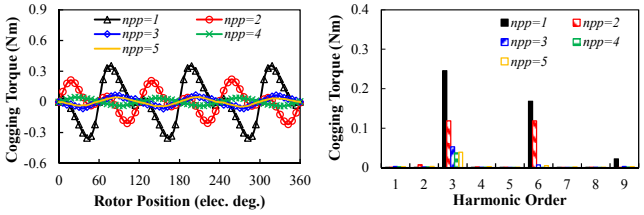

Fig. 18. Cogging torques. (a) Waveforms. (b) Harmonic spectra.

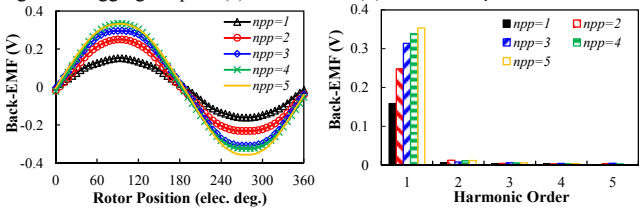

Fig. 19. Back-EMFs. (a) Waveforms. (b) Harmonic spectra.

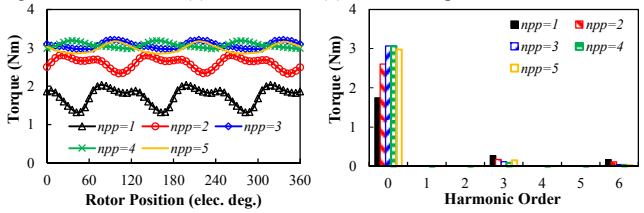

Fig. 20. Rated torques. (a) Waveforms. (b) Harmonic spectra.

analytically predicted torque values are also calculated based on the parameters of the optimum FEA models. As can be seen, for N_s=6, the FEA and analytical results match well with each other while for other N_s, the analytical value is slightly smaller than the FEA value, which is mainly attributed to the assumptions made in the analytical model. More importantly, for both FEA and analytical results, the optimal *npp* is 3 for N_s=6, while it is 2 for N_s=12 and 1 for N_s =18 and 24. Therefore, the previous analysis of the optimal *npp* is verified by FEA.

For N_s=6, the detailed parameters of the optimum FEA models are shown in TABLE IV. It should be noted that although the optimal PM heights for all *npp* are smaller than 2mm so as to reduce the equivalent air-gap length, they all selected as 2mm to guarantee the mechanical strength and anti-demagnetization capability of PMs. Besides, the optimal split ratio increases with *npp* while the width ratio of stator slot opening decreases with *npp*. Again, these phenomena match well with the previous analysis.

Fig. 17 shows the cross-sections and flux distributions of these optimal machine models. Despite different *npp*, the flux distributions are similar for the five models especially in stator and rotor yoke. Fig. 18 shows the cogging torques of the five machines. As can be seen, the fundamental periods of cogging torques are all 3, but the magnitude firstly decreases with *npp* and achieves the minimum value when *npp*=4, which is consistent with Fig. 8. Fig. 19 shows the back-EMFs of the machines at n=400rpm (the winding turns per phase N_{ph} are 4). It shows that the fundamental back-EMF is largely improved by 98% when *npp* increases from 1 to 3. By further increasing *npp*, the fundamental back-EMF still slightly increases because of the increased split ratio (see TABLE IV). Fig. 20 shows the rated torques of the machines when the copper loss p_{cu}=20W.

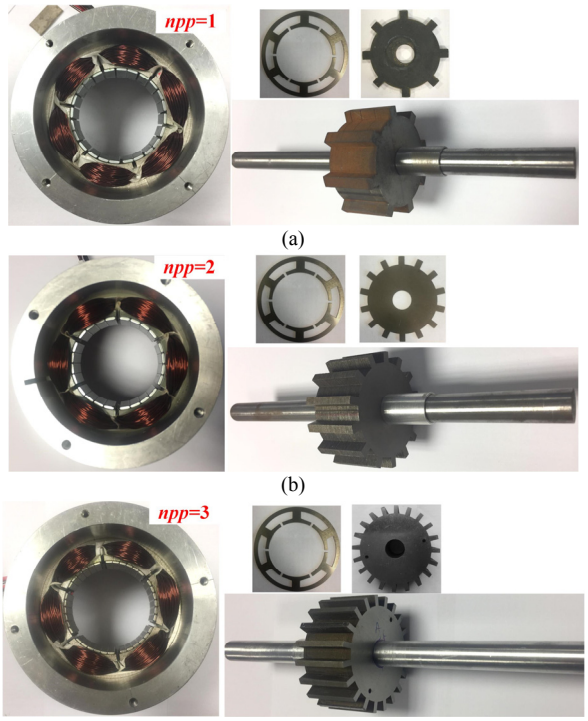

Fig. 21. Prototype machines (N_s=6). (a) *npp*=1. (b) *npp*=2. (c) *npp*=3.

As can be seen, the average torque firstly increases with *npp*, and can be improved by 76% when *npp* changes from 1 to 3. Meanwhile, the torque ripple reduces from 41% to 8%, thanks to the reduced cogging torque. When *npp* is further increased from 3, the average torque starts to decrease. Therefore, the optimal *npp* of 3 for N_s=6 is verified.

VI. Experimental Validation

To further verify the conclusions aforementioned, 6-slot-stator prototype machines with different *npp* are manufactured, and their parameters are listed in TABLE IV. Since the machine overall diameter is relatively small (D=90mm), only three prototypes (*npp*=1, 2 and 3) are made to ease manufacturing and assembling of PMs and salient rotor. For simplicity, three machines share the same stator lamination, and for *npp*=1, 2, four PM pieces are mounted on each stator tooth. However, for *npp*=1, the polarities of four PM pieces are arranged as N-N-S-S, while that are arranged as N-S-N-S for *npp*=2, as shown in Fig. 21 (a), (b). The number of turns per coil is 115 for all the machines. In addition, for *npp*=1, the rotor pole number N_r is 8, as shown in Fig. 21 (a); for *npp*=2, N_r=14, as shown in Fig. 21 (b); for *npp*=3, N_r=20, as shown in Fig. 21(c).

Fig. 22 (a) shows the measured and FE-predicted back-EMF waveforms of the machines when n=400rpm, while their harmonic spectra are shown in Fig. 22(b). As can be seen, good agreement is achieved between the results especially for small *npp*, and the relatively large difference between measured and FE-predicted results for *npp*=3 (with the magnitude difference of fundamental back-EMFs being 14%) is attributed to the end-effect and manufacturing tolerance since the numbers of

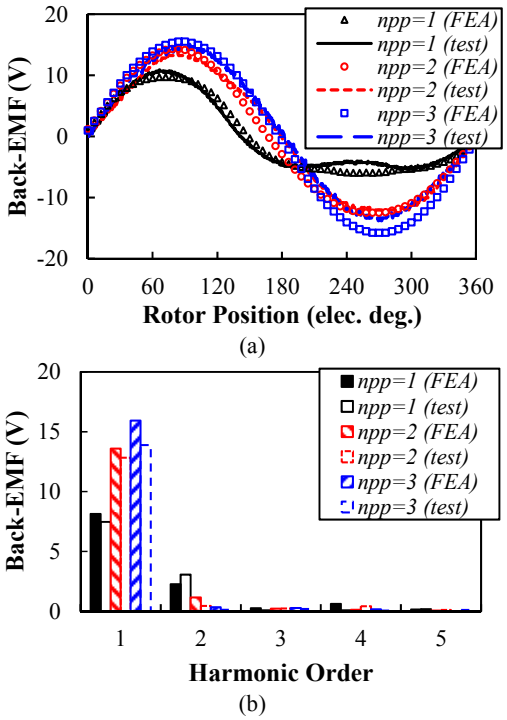

Fig. 22. Measured and FE-predicted back-EMFs (n=400rpm). (a) Waveforms. (b) Harmonic spectra.

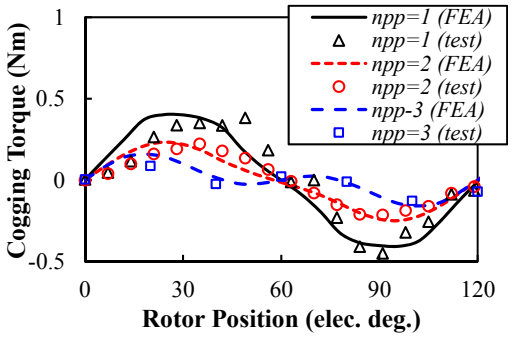

Fig. 23. Measured and FE-predicted cogging torques.

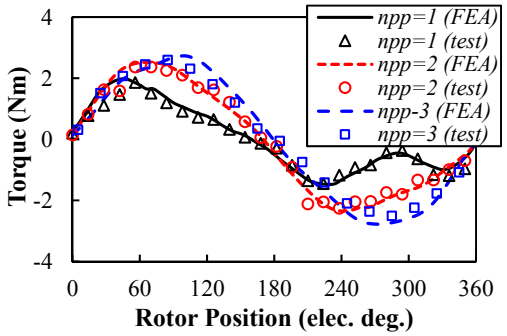

Fig. 24. Measured and FE-predicted static torques (I_a=-2I_b=-2I_c).

PM pieces and rotor pole are high. In addition, for *npp*=1, the back-EMF waveforms are asymmetric due to the large even harmonics, and *npp*=3 has the maximum measured fundamental back-EMF (improved by 82% compared to *npp*=1).

By using the simple cogging torque measurement method introduced in [25], Fig. 23 shows the measured and

FE-predicted cogging torques of the machines. Due to the high rotor pole number and corresponding limited torque measurement point, only cogging torque waveforms are given. However, it can be clearly seen that the fundamental periods of the cogging torque of the machines are same but the peak to peak value decreases with *npp*, which is consistent with the previous conclusions.

The variation of static torque with rotor position is measured by supplying three-phase windings with fixed dc current (I_a=-2I_b=-2I_c=I_{dc}=I_{rated}, and the rated current I_{rated} is corresponded to p_{cu}=20W) [22]. Fig. 24 shows the measured and FE-predicted static torques of the machines. As can be seen, the measured static torque waveforms match well with the FE-predicted waveforms. With rated current injected, the maximum measured torque of *npp*=3 is the largest, which is 40% larger than that of *npp*=1.

VII. Conclusion

In this paper, the influence of number of PM pieces on the electromagnetic performance of FRPM machines is analyzed, from which the optimal number of PM pieces is identified. The analytical expressions of machine performance are firstly derived, revealing that there exists an optimal *npp* value to maximize the output torque. When N_s=6, compared with the conventional machine with *npp* being 1, the machine with the optimal *npp* of 3 has 82% higher back-EMF. It is revealed that the improved performance is mainly because of the additional contribution by *Auxiliary* PM MMF. Besides, the influence and design guidance of some key design parameters including stator slot opening ratio, split ratio and stator slot number are analyzed. Results show that the FRPM machines with optimal number of PM pieces exhibits advantage especially for small stator slot numbers. In addition, both FEA and experimental results are used to verify the analytical findings.

References

[1] Z. Q. Zhu and D. Howe, "Electrical machines and drives for electric, hybrid, and fuel cell vehicles," *Proc. IEEE,* vol. 95, no.4, pp. 746-765, Apr. 2007.

[2] J. Cros and P. Viarouge, "Synthesis of high performance PM motors with concentrated windings," *IEEE Trans. Energy Convers.*, vol. 17, no. 2, pp. 248–253, Jun. 2002

[3] J. X. Shen, H. Y. Li, H. Hao, and M. J. Jin, "A coaxial magnetic gear with consequent-pole rotors," *IEEE Trans. Energy Convers.*, vol. 32, no. 1, pp. 267–275, Mar. 2017.

[4] M. Cheng, W. Hua, J. Zhang, and W. Zhao, "Overview of stator-permanent magnet brushless machines," *IEEE Trans. Ind. Electron.*, vol. 58, no. 11, pp. 5087–5101, Nov. 2011.

[5] Y. Guo, J. G. Zhu, P. A. Watterson, and W. Wu, "Development of a PM transverse flux motor with soft magnetic composite core," *IEEE Trans. Energy Convers.*, vol. 21, no. 2, pp. 426–434, Jun. 2006.

[6] K. T. Chau, D. Zhang, J. Z. Jiang, C. H. Liu, and Y. J. Zhang, "Design of a magnetic-geared outer-rotor permanent-magnet brushless motor for electric vehicles," *IEEE Trans. Magn.*, vol. 43, no. 6, pp. 2504–2506, Jun. 2007.

[7] A. Toba and T. A. Lipo, "Generic torque-maximizing design methodology of surface permanent-magnet Vernier machine," *IEEE Trans. Ind. Appl.*, vol. 36, no. 6, pp. 1539–1545, Nov./Dec. 2000.

[8] Z. Q. Zhu, "Overview of novel magnetically geared machines with partitioned stators," *IET Electr. Power Appl.*., vol. 12, no. 5, pp. 595–604, Apr. 2018

[9] Y. Liao, F. Liang, and A. Lipo, "A novel permanent magnet motor with doubly salient structure," *IEEE Trans. Ind. Appl.*, vol. 31, no. 5, pp. 1069–1078, Sep.-Oct. 1995.

[10] E. Hoang, A. H. Ben-Ahmed, and J. Lucidarme, "Switching flux permanent magnet polyphased synchronous machines," in *Proc. 7th Eur. Conf. Power Electronics and Applications*, vol. 3, 1997, pp. 903–908.

[11] R. Deodhar, S. Andersson, I. Boldea, and T. J. E. Miller, "The flux reversal machine: A new brushless doubly-salient permanent magnet machine," *IEEE Trans. Ind. Appl.*, vol. 33, no. 4, pp. 925–934, Jul. 1997.

[12] D. S. More and B. G. Fernandes, "Power density improvement of three phase flux reversal machine with distributed winding," *Proc. IET*, *Electr. Power Appl.*, vol. 4, no. 2, pp. 109–120, Feb. 2010.

[13] Y. Gao, R. Qu, D. Li, J. Li, and L. Wu, "Design of three-phase flux-reversal machines with fractional-slot windings," *IEEE Trans. Ind. Appl.*, vol. 52, no. 4, pp. 2856–2864, July 2016.

[14] Z. Q. Zhu, Z. Z. Wu, D. Evans, and W. Q. Chu, "Novel electrical machines having separate PM excitation stator," *IEEE Trans. Magn.*, vol. 51, no. 4, Apr. 2015, Art. ID 8104109.

[15] T. H. Kim, "A study on the design of an inset-permanent-magnet-type flux-reversal machine," *IEEE Trans. Magn.*, vol. 45, no. 6, pp. 2859–2862, May 2009.

[16] Y. Gao, R. Qu, D. Li, J. Li, and G. Zhou, "Consequent-pole flux-reversal permanent-magnet machine for electric vehicle propulsion," *IEEE Trans. Appl. Supercond.*, vol. 26, no. 4, Jun. 2016.

[17] D. Li, Y. Gao, R. Qu, J. Li, Y. Huo, and H. Ding, "Design and analysis of a flux reversal machine with evenly distributed permanent magnets," *IEEE Trans. Ind. Appl.*, vol. 54, no. 1, pp. 172–183, Jan. 2018.

[18] H. Li and Z. Q. Zhu, "Influence of magnet arrangement on performance of flux reversal permanent magnet machine," in *Electr. Mach. Drives (IEMDC 2017)*, *IEEE Int. Conf.*, May 2017.

[19] C. Wang, S. A. Nasar, and I. Boldea, "Three-phase flux reversal machine (FRM)," *Proc. Inst. Elect. Eng.—Electr. Power Appl.*, vol. 146, no. 2, pp. 139–146, Mar. 1999.

[20] I. Boldea, J. Zhang, and S. A. Nasar, "Theoretical characterization of flux reversal machine in low speed servo drives-the pole-PM configuration," *IEEE Trans. Ind. Appl.*, vol. 38, no. 6, pp. 1549–1557, Dec. 2002.

[21] D. S. More and B. G. Fernandes, "Analysis of flux-reversal machine based on fictitious electrical gear," *IEEE Trans. Energy Convers.*, vol. 25, no. 4, pp. 940–947, Dec. 2010.

[22] Y. Gao, R. Qu, D. Li, and J. Li, "Torque performance analysis of three-phase flux reversal machines," *IEEE Trans. Ind. Appl.*, vol. 53, no. 3, pp. 2110–2119, Mar. 2017.

[23] H. Y. Li, Y. Liu, and Z. Q. Zhu, "Comparative study of air-gap field modulation in flux reversal and vernier permanent magnet machines," *IEEE Tran. Magn*., in press.

[24] Z. Q. Zhu and D. Howe, "Instantaneous magnetic field distribution in brushless permanent magnet dc motors, part III: Effect of stator slotting," *IEEE Trans. Magn.*, vol. 29, no. 1, pp. 143–151, Jan. 1993.

[25] Z. Q. Zhu, "A simple method for measuring cogging torque in permanent magnet machines," in *Proc. IEEE Power Energy Soc. Gen. Meet.*, 2009, pp. 1–4.

Hua-Yang Li was born in Shanxi, China, in 1992. He received the B.Eng. and M.Sc. degrees in electrical engineering from Zhejiang University, Hangzhou, China, in 2013 and 2016, respectively. He is currently pursuing the Ph.D. degree at The University of Sheffield, Sheffield, U.K. His research interests include design and analysis of magnetic gears and permanent magnet machines.

Z.Q. Zhu received the B.Eng. and M.Sc. degrees in electrical and electronic engineering from Zhejiang University, Hangzhou, China, in 1982 and 1984, respectively, and the Ph.D. degree in electrical and electronic engineering from The University of Sheffield, Sheffield, U.K., in 1991.

Since 1988, he has been with The University of Sheffield, where he is currently a Professor with the Department of Electronic and Electrical Engineering,

Head of the Electrical Machines and Drives Research Group, Royal Academy of Engineering/Siemens Research Chair, Academic Director of Sheffield Siemens Wind Power Research Centre, Director of Midea Electrical Machines and Controls Research Centres, Director of Sheffield CRRC Electric Drives Technology Research Centre. His current major research interests include the design and control of permanent-magnet brushless machines and drives for applications ranging from automotive through domestic appliance to renewable energy. Prof. Zhu is Fellow of Royal Academy of Engineering, Fellow of IEEE, and Fellow of IET.